

Cellulose microfibril crystallinity is reduced by mutating C-terminal transmembrane region residues CESA1^{A903V} and CESA3^{T942I} of cellulose synthase

Darby M. Harris^a, Kendall Corbin^a, Tuo Wang^b, Ryan Gutierrez^c, Ana L. Bertolo^d, Carloalberto Petti^a, Detlef-M. Smilgies^e, José Manuel Estevez^f, Dario Bonetta^g, Breeanna R. Urbanowicz^{d,1}, David W. Ehrhardt^c, Chris R. Somerville^{h,2}, Jocelyn K. C. Rose^d, Mei Hong^b, and Seth DeBolt^{a,2}

^aDepartment of Horticulture, University of Kentucky, Lexington, KY 40546; ^bDepartment of Chemistry and Ames Laboratory, Iowa State University, Ames, IA 50011; ^cDepartment of Plant Biology, Carnegie Institution for Science, Stanford, CA 94305; ^dDepartment of Plant Biology, Cornell University, Ithaca, NY 14853; ^eCornell High Energy Synchrotron Source (CHESS) Wilson Laboratory, Cornell University, Ithaca, NY 14853; ^fInstituto de Fisiología, Biología Molecular y Neurociencias, Universidad de Buenos Aires, Buenos Aires C1428EGA, Argentina; ^gFaculty of Science, University of Ontario Institute of Technology, ON Canada L1H 7K4; and ^hDepartment of Plant and Microbial Biology, University of California, Berkeley, CA 94720

Contributed by Chris R. Somerville, January 8, 2012 (sent for review November 28, 2011)

The mechanisms underlying the biosynthesis of cellulose in plants are complex and still poorly understood. A central question concerns the mechanism of microfibril structure and how this is linked to the catalytic polymerization action of cellulose synthase (CESA). Furthermore, it remains unclear whether modification of cellulose microfibril structure can be achieved genetically, which could be transformative in a bio-based economy. To explore these processes *in planta*, we developed a chemical genetic toolbox of pharmacological inhibitors and corresponding resistance-conferring point mutations in the C-terminal transmembrane domain region of CESA1^{A903V} and CESA3^{T942I} in *Arabidopsis thaliana*. Using ¹³C solid-state nuclear magnetic resonance spectroscopy and X-ray diffraction, we show that the cellulose microfibrils displayed reduced width and an additional cellulose C4 peak indicative of a degree of crystallinity that is intermediate between the surface and interior glucans of wild type, suggesting a difference in glucan chain association during microfibril formation. Consistent with measurements of lower microfibril crystallinity, cellulose extracts from mutated CESA1^{A903V} and CESA3^{T942I} displayed greater saccharification efficiency than wild type. Using live-cell imaging to track fluorescently labeled CESA, we found that these mutants show increased CESA velocities in the plasma membrane, an indication of increased polymerization rate. Collectively, these data suggest that CESA1^{A903V} and CESA3^{T942I} have modified microfibril structure in terms of crystallinity and suggest that in plants, as in bacteria, crystallization biophysically limits polymerization.

cell wall | polysaccharide | quinoxiphen

The fundamental unit comprising naturally produced cellulose is the *para*-crystalline microfibril, which consists of multiple parallel chains of unbranched β -1,4-glucan that aggregate via hydrogen bonds and van der Waals forces. Cellulose-synthesizing organisms typically produce microfibrils from large plasma membrane (PM)-localized cellulose-synthesizing complexes (CSCs) (1). The geometry of CSCs range from either linear arrays of particles with single rows, as seen in the bacterium *Gluconacetobacter xylinus* [formerly *Acetobacter xylinus*(*m*)], to multiple rows, as found in the green alga *Oocystis apiculata*, to hexagonal arrays of particles termed rosettes that occur in Charophycean algae and all land plants (2). The arrangement of particles within the CSCs of these and other organisms has been correlated with the size and shape of the cellulose microfibrils that they produce (2). A detailed analysis of microfibril structure has revealed the existence of two crystalline allomorphs of naturally occurring cellulose, cellulose I α (triclinic unit cell) and I β (monoclinic unit cell) (3). The elucidation of the crystal structure of both forms has helped determine the hydrogen-bonding network within and between glucan chains as well as between sheets of chains so

formed (4, 5). Analysis of higher plant cellulose suggests not only the presence of large numbers of ordered and disordered crystal-surface chains (6), but that the inner chains of the microfibril core are more crystalline, while more amorphous forms of cellulose compose the chains in the surrounding *para*-crystalline sheath (7). These analyses have raised the question that if the geometry of the CSC determines the lateral dimensions of the microfibril (8), then does it also determine microfibril structure or is this feature instead dictated by glucan chain self-assembly?

Pioneering studies with the bacterium *A. xylinum* have shown that the fluorescent dye Calcofluor disrupts the crystallization of cellulose by hydrogen bonding to individual glucan chains immediately upon their emergence from the cell, thereby preventing their assembly into a microfibril (9). The disruption of microfibril assembly caused an increase in the rate of glucan chain polymerization, suggesting that the two processes are biophysically coupled and that crystallization is rate limiting (10). However, during plant cellulose biosynthesis, it remains unclear whether a link exists between cellulose crystallization and the CSC function in terms of polymerization. This is in part due to a lack of low-crystallinity cellulose mutants available to explore this postulate. Moreover, in plant cells as opposed to bacteria, the requirement for cellulose production is not dispensable and is linked to the anisotropic expansion of the cell and assaying polymerization after pharmacological decrystallization is complicated by the inherent fluorescence of the β -glucan binding dye Calcofluor (11).

In *Arabidopsis*, 10 *CESA* genes have been identified (12). A combination of biochemical and genetic analyses has shown that at least three cellulose synthase (CESA) subunits directly interact to form a CSC during primary (13, 14) and secondary (15) cell wall cellulose formation. The temperature-sensitive mutation (or homozygous allele) *rsw1-1* (*CESA1*) results in primary wall deficiencies accompanied by a disappearance of rosettes from the membrane at the nonpermissive temperature (16), and strong homozygous alleles are either male gametophyte or embryo lethal (14, 17). *CESA3* is coexpressed with *CESA1*, and null homozygous *cesa3* alleles are also male gametophyte lethal (14). The remaining

Author contributions: D.M.H., A.L.B., D.B., B.R.U., D.E., C.R.S., J.K.C.R., M.H., and S.D. designed research; D.M.H., K.C., T.W., R.G., A.L.B., C.P., J.M.E., D.B., B.R.U., M.H., and S.D. performed research; T.W., A.L.B., D.-M.S., and M.H. contributed new reagents/analytic tools; D.M.H., T.W., R.G., A.L.B., J.M.E., D.B., B.R.U., D.E., J.K.C.R., M.H., and S.D. analyzed data; and D.M.H., R.G., D.E., C.R.S., J.K.C.R., M.H., and S.D. wrote the paper.

The authors declare no conflict of interest.

¹Present address: Complex Carbohydrate Research Center: University of Georgia, Athens, GA 30602.

²To whom correspondence may be addressed. E-mail: crs@berkeley.edu or sdebo2@uky.edu.

This article contains supporting information online at www.pnas.org/lookup/suppl/doi:10.1073/pnas.1200352109/-DCSupplemental.

primary cell wall *CESA* genes display a degree of redundancy (13, 14). In addition to *CESA*, several other genes have been linked to a role in cellulose biosynthesis by null alleles resulting in cellulose deficiency (18). Recent studies with *CESA* fused to fluorescent reporter proteins suggest that CSCs move at relatively stable trajectories at the PM via a microtubule (MT) guidance mechanism (19). However, when MTs are completely depolymerized, relative *CESA* velocity remains unchanged in otherwise wild-type (WT) plants, suggesting that energy provided by glucan chain polymerization is primarily responsible for movement rather than MT motor proteins (19, 20). The effect that genetic mutations have on cellulose polymerization rates can therefore be explored by examining the displacement velocity of fluorescently labeled *CESA* at the PM. Although previous analyses of the *CESA* velocity in cellulose deficient or MT mutants have suggested that polymerization rate can be altered, these studies have not addressed the influence that microfibril structure could impart on *CESA* velocity (21–24).

Here, we identified a mutant, *CESA1*^{A903V} (*cesa1*^{aegeus}) by forward chemical genetics and created a double mutant with the previously identified *CESA3*^{T942I} (*cesa3*^{ixr1-2}) (25). X-ray diffraction (XRD) and ¹³C solid-state nuclear magnetic resonance (SSNMR) spectroscopy are employed to show that *cesa1*^{aegeus} and *cesa3*^{ixr1-2} confer changes to the ordered crystallization of glucan chains in the interior of cellulose microfibrils. Lower crystallinity cellulose displays greater digestibility characteristics relative to WT and reveals a consistent coupled association between crystallization and polymerization that is conserved between bacterial (10) and plant cellulose biosynthetic processes.

Results

Identification and Characterization of the Cellulose Biosynthesis Inhibitor Quinoxiphen. The herbicide quinoxiphen (Fig. 1A; Fig. S1) was identified in a screen for compounds that inhibit cell growth anisotropy. Germination on quinoxiphen above the IC₅₀ value of 1.0 μM caused severe cell and tissue swelling of the hypocotyl and upper root in *Arabidopsis* seedlings (Fig. 1B). In addition, there was a 50% inhibition of ¹⁴C-glucose incorporation into crystalline cellulose in plants germinated and grown on a 5.0 μM concentration of quinoxiphen (Fig. 1C). Differences in cell wall composition based on FTIR spectra were detected in quinoxiphen treated seedlings (Fig. S2A and B), as well as significant increases in the abundance of cell wall neutral sugars (Fig. S2C). Additional analysis of seedlings exposed to quinoxiphen showed other cell wall compositional alterations, including hyper-accumulation of callose and ectopic lignin production; both common phenotypes observed following chemical inhibition of cellulose biosynthesis (25, 26) (Fig. S3A–D).

In expanding *Arabidopsis* hypocotyl tissue, cellulose biosynthesis can be visualized in living cells by labeling the CSC with fluorescently tagged *CESA* proteins. To establish a possible cause of the anisotropic growth disruption and cellulose content reduction, we used spinning disk confocal microscopy to examine the effect of quinoxiphen on the behavior of YFP-*CESA6* particles in the focal plane of the PM. Consistent with previous observations, following treatment with the herbicide isoxaben (19), CSCs were depleted from the PM, a change visualized in time-projected images by the loss of tracks created by particle translocation (Fig. 1D). Concurrently, label accumulated in trafficking compartments at the cell cortex, most of which were immobilized (Fig. 1D, see ref. 27 for further analysis of this redistribution syndrome). In contrast, no marked differences in morphology or general dynamics were observed in actin or MT cytoskeletons after quinoxiphen treatment (Fig. S4). Hence, we hypothesized that quinoxiphen targets cellulose biosynthesis, rather than causing broad cell toxicity, and that its mechanism of action is similar to that of isoxaben.

Resistance to Quinoxiphen Is Conferred by a Semidominant *CESA1* Allele. To identify possible targets of quinoxiphen, we performed

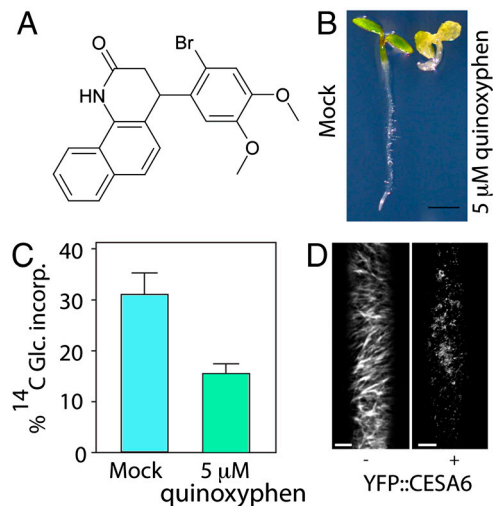


Fig. 1. Identification of quinoxiphen as a cellulose biosynthesis inhibitor. (A) Structure of 4-(2-bromo-4,5-dimethoxyphenyl)-3,4-dihydro-1H-benzoquinolin-2-one (C₂₁H₁₈BrNO₃ MW 412.28), named herein quinoxiphen. (B) *Arabidopsis* seedlings grown under continuous light for 5 d on MS agar containing 5 μM quinoxiphen (Right) showed reduce growth compared with control plant (Left). Scale bar, 10 mm. (C) Incorporation of ¹⁴C-glucose in the acid-insoluble fraction in WT treated and untreated with 5.0 μM quinoxiphen. (**P* < 0.001, Student's *t* test, *n* = 3 with 200 seedling per replicate). (D) Time-lapse confocal images of YFP::CESA6 in hypocotyl cells of 3-d-old etiolated plants were compared between mock control treatment and 20 μM quinoxiphen treatment revealing clearance of the PM CSCs after 120 min. Each image in D is an average of 60 frames taken at 5-s intervals on the same Z plane (*n* = 3). Scale bar, 10 μm.

a forward genetic screen and isolated an *Arabidopsis* mutant showing strong resistance to quinoxiphen (>10 mM), which we named *aegeus* (Fig. 2A). Given the similar phenotypes induced by quinoxiphen and isoxaben, as observed with live-cell imaging, we tested whether the two drugs shared the same resistance locus. In an allelism test between *aegeus* and the isoxaben resistant mutant *ixr1-2*, the F1 progeny from crosses between the two homozygotes showed sensitivity when germinated and grown in media containing 5 μM of quinoxiphen or 10 nM of isoxaben (both lethal doses to WT), indicating that the two resistance loci were not allelic. In addition, homozygous *aegeus* plants displayed sensitivity to isoxaben, and homozygous *ixr1-2* plants were sensitive to quinoxiphen. Using a positional cloning approach to identify the gene conferring resistance to quinoxiphen, we found that the *aegeus* mutation corresponds to the replacement of an alanine with a valine in the fourth transmembrane spanning domain at amino acid position 903 in the C-terminal end of the *CESA1* protein (Fig. 2B and C). The mutated alanine is not highly conserved among primary cell wall *CESAs*, but is flanked by several highly conserved residues (Fig. 2C). The *aegeus* mutant displayed semidominant inheritance similar to that observed for isoxaben resistance in the *ixr* mutants (25, 26). Both *cesa1*^{aegeus} and *cesa3*^{ixr1-2} occur within the C-terminal region of *CESA* proteins comprising six transmembrane domains, and both occur in essential genes for cellulose biosynthesis in the primary wall (Fig. 2B (14, 16). Complementation of *cesa1*^{aegeus} by transformation with WT *CESA1* restored sensitivity to quinoxiphen.

Generation of Double Drug-Resistant Mutants. We generated the double mutant *cesa1*^{aegeus}/*cesa3*^{ixr1-2}, thereby creating a primary cell wall CSC containing two essential *CESA* subunits with mutations conferring drug resistance. The double mutant showed resistance to both quinoxiphen and isoxaben, but also a far more pronounced dwarf phenotype than either of the single mutants (Fig. S2D–F). Significant differences were also apparent during

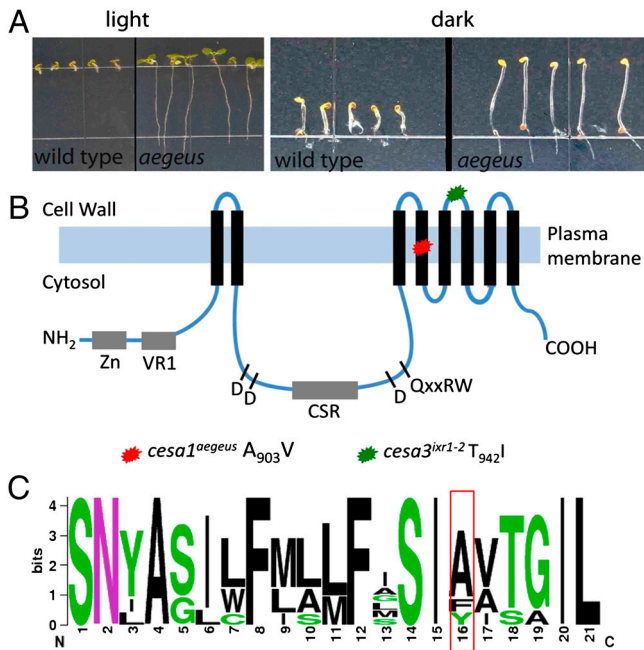


Fig. 2. The *aegeus* mutant is resistant to quinoxiphen. (A) The phenotype of the *aegeus* mutant compared to WT when grown for 7 d in the light (Left) or the dark (Right) on media containing 5 μ M quinoxiphen ($n = 5$). (B) The gene corresponding to the *aegeus* mutation was cloned using a map-based approach (Fig. S3 and Table S2) and revealed an alanine to valine change at position 903 in the AtCESA1 protein (At4g3241). (C) Sequence logo assessment of residues in the fourth transmembrane domain of primary cell wall CESA proteins illustrates the location and conservation of the mutated alanine residue in CESA1 (red box). Amino acids are colored according to their chemical properties: Polar amino acids are green, basic are blue, acidic are red, and hydrophobic are black.

the first 7 d of dark-grown hypocotyl elongation (Fig. S2F and Fig. S5b) and in light-grown root growth (Fig. S5A and C). Examination of crystalline cellulose content of mature stem and dark-grown hypocotyls revealed a significant reduction in all mutants compared with WT (Table 1).

To dissect the structure of the cell wall in these mutants, we combined neutral sugar analysis, glycosidic linkage analysis (Tables S1 and S2) and ^{13}C SSNMR (Fig. 3). Neutral sugar composition analysis revealed significant differences in neutral sugars as a proportion of total cell wall (Table S1). In addition, although there was little to no hyper-accumulation of callose in the mutant hypocotyls (Fig. S3E–H), similar to quinoxiphen treatment, the double mutant *cesa1aegeus/cesa3ixr1-2* showed increased ectopic lignin production (Fig. S3I–L). Quantitative ^{13}C SSNMR spectra of uniformly ^{13}C labeled cell walls indicated increased intensities

Table 1. Effect of mutation on cellulose content and crystallite size

| Genotype | Cellulose content, $\mu\text{g}/\text{mg}$ AIR | | |
|--------------------------------|---|-----------------|--|
| | Hypocotyls | Stems | Crystallite size, $\text{\AA} \pm \text{SE}$ |
| WT | 415 \pm 20.8 | 217 \pm 6.5 | 23.4 \pm 0.26 |
| <i>cesa1aegeus</i> | 249 \pm 13.4* | 146 \pm 7.2* | 21.9 \pm 0.35* |
| <i>cesa3ixr1-2</i> | 297 \pm 6.8* | 150 \pm 13.7* | 22.0 \pm 0.48* |
| <i>cesa1aegeus/cesa3ixr1-2</i> | 161 \pm 6.3* | 140 \pm 12.0* | 22.5* \pm 0.34* |

Asterisks in cellulose measurements of dark-grown hypocotyls and mature stems indicate $P < 0.001$ Student's t test, $n = 3$. Cellulose content presented as μg cellulose per mg acetone insoluble residue (AIR). Mutant and WT plants were grown to maturity, and the first internode of the stem was exposed to synchrotron X-ray analysis to measure crystallite size (lateral dimensionality). Asterisks indicate $P < 0.01$ Student's t test, $n = 4$.

of pectin and hemicellulose peaks relative to the interior cellulose C4 peak at 89 ppm for all mutants (Fig. 3A and B). For example, the arabinan (Ara) C1 signal at 108 ppm, the galacturonic acid (GalA) and rhamnose (Rha) C1 signal at 101 ppm, and the C2/C4 signals of xyloglucan (XG) Glc, GalA, Rha, and the Ara signals at 80–83 ppm, increased markedly, consistent with linkage analysis (Fig. S6A and B and Table S2). The relative amounts of glycoprotein to interior cellulose also increased in the mutants by about twofold compared to WT. Hence, the *cesa1aegeus*, *cesa3ixr1-2*, and *cesa1aegeus/cesa3ixr1-2* display quantitatively less cellulose and relative increases in pectin, hemicellulose and glycoprotein as a proportion of the cell wall.

***cesa1aegeus* and *cesa3ixr1-2* Mutations Cause Increased Cellulose Synthase Movement in the PM.** We examined the in vivo behavior of the CSC complexes in the *aegeus* mutant, with and without the *ixr1-2* mutation, by creating double and triple mutants in stable transgenic plants expressing fluorescent reporters, and using spinning disk laser confocal microscopy to visualize the movement of the CSCs in living cells. Bidirectional trajectories of fluorescent CSCs were visualized at the PM focal plane of dark-grown transgenic seedlings in all mutant combinations (epidermal cells in the upper hypocotyl; Fig. 4A and Fig. S4). The relative mean velocity of labeled CESA complexes was significantly greater in *cesa1aegeus*, *cesa3ixr1-2*, and the double mutant than in transgenic lines that carried WT alleles of *CESA1* and *CESA3* ($P < 0.0001$, ANOVA with Bonferroni tests) (Fig. 4A). Previously, increased polymerization rates were observed in studies of bacterial cellulose synthesis, where the pharmacological disruption of crystallization prevented microfibril assembly and caused an increased polymerization rate (9, 10). Based on the difference in CESA behavior (Fig. 4A), and prior evidence from bacteria, we postulated that cellulose microfibril structure may be aberrant in *cesa1aegeus* and *cesa3ixr1-2* mutants, and may reflect differences in cellulose crystallization.

***cesa1aegeus*, *cesa3ixr1-2*, and *cesa1aegeus/cesa3ixr1-2* Mutants Produce Structurally Aberrant Cellulose Microfibrils.** As an initial experiment, we measured the relative crystallinity index (RCI) for each sample using XRD based on the Segal method (28). This assay is incapable of determining any accurate structural information for the cellulose crystallites and instead reflects the proportion of crystalline to amorphous cell wall components (29, 30). *cesa1aegeus*, *cesa3ixr1-2*, and *cesa1aegeus/cesa3ixr1-2* all show significantly reduced RCI values compared to WT (Fig. 4B). However, as indicated by the ^{13}C SSNMR analysis, the hemicellulose fraction relative to interior cellulose also increased in the mutants, which will contribute to the amorphous peak present in the XRD data and skew the RCI determination toward lower crystallinity. Therefore, to obtain a more accurate estimation of the microfibril structure, we examined the first internode of mature stem using high-energy synchrotron radiation XRD and obtained an estimation of the crystallite width using the Scherrer equation (31). This method allows the examination of intact plant samples, and so disruptive grinding or chemical treatments are unnecessary. Synchrotron XRD data indicated a significant reduction in the crystallite width for *cesa1aegeus*, *cesa3ixr1-2*, and *cesa1aegeus/cesa3ixr1-2* compared to WT (Table 1). However, within biomass samples the use of ^{13}C SSNMR is required to delineate accurate structural information about cellulose (32, 33).

Further analysis of the actual crystallite structure was obtained from quantitative ^{13}C SSNMR spectra of uniformly ^{13}C -labeled cell wall (Fig. 3A). Based on the intensity ratio of interior C4 (iC4) (88.5–91.5 ppm) to surface C4 (sC4) (84–86 ppm) peak intensities, we found that the double mutant had 8% lower crystallinity relative to WT (Table S3), while the single mutants had smaller differences from the WT. The mutants also displayed additional intensities in the regions of the iC4 peak, with a new

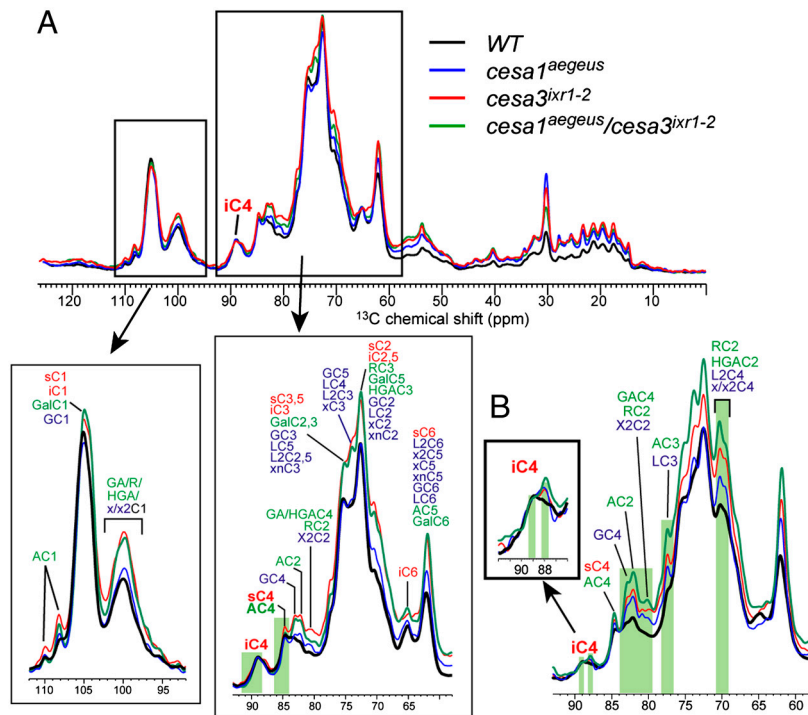


Fig. 3. ^{13}C magic-angle-spinning SSNMR analysis of cellulose and cell wall structure in *cesa1^{aegeus}*, *cesa3^{ixr1-2}*, and *cesa1^{aegeus}/cesa3^{ixr1-2}*. (A) Quantitative ^{13}C magic-angle-spinning SSNMR spectra of WT and mutant cell walls. The intensity ratio of interior (88.5–91.5 ppm) to surface (84–86 ppm) cellulose C4 peaks was the lowest for the double mutant. The relative amount of hemicellulose and pectin signals to interior cellulose is significantly higher in all mutants compared to WT. The spectra were measured quantitatively by ^{13}C direct polarization using a long recycle delay of 20 s. (B) ^{13}C direct-polarization spectra measured with a short recycle delay of 2 s, which preferentially enhances the signals of mobile polysaccharides. The hemicellulose and pectin signals and the 88-ppm less-crystalline cellulose signal are increased for the mutants relative to the WT.

88-ppm peak that is largely absent in the WT spectrum (Fig. S6). This 88-ppm peak is closer to the 85-ppm C4 peak of the more amorphous surface cellulose, suggesting that it corresponds to less crystalline cellulose (Fig. 3B, *Inset*). Further, the 88-ppm intensity is preferentially enhanced in the mutant samples relative to the WT when the ^{13}C spectra were measured using short recycle delays to increase the intensities of dynamic polysaccharides. This suggests that the less crystalline glucan chains in the mutants are more dynamic, which is consistent with weakened hydrogen bonding and the amorphous nature of the chains. In 2D double-quantum correlation spectra, we also observed two types of interior cellulose, which were best resolved in the *CESA3^{ixr1-2}* mutant but were also present in the other mutants (Fig. S6). Therefore, in the mutants, the microfibrils displayed reduced width and an additional cellulose C4 peak indicative of a degree of crystallinity that is intermediate between the surface and interior cellulose of WT, suggesting a difference in glucan chain association during microfibril formation.

We tested whether cellulose with more mobile amorphous iC4 intensity might show differences in saccharification efficiency when hydrolyzed with cellulase enzymes, as cellulose crystallinity has been shown to be an important predictor of enzymatic hydrolysis rate (34). The catalytic efficiency ($\text{app}V_{\text{max}}/K_m$) value showed a 32% and 49% increase in hydrolytic efficiency when using the *cesa1^{aegeus}* and *cesa1^{aegeus}/cesa3^{ixr1-2}* cellulose extracts, respectively (Fig. S5), consistent with our prior examination of *cesa3^{ixr1-2}* (35). These saccharification data support the quantitative ^{13}C SSNMR spectra, indicating increased mobile iC4 assignments, from which we deduce that the amino acid sequence of the *cesa1^{aegeus}* and *cesa3^{ixr1-2}* has an important influence on cellulose microfibril architecture.

Discussion

It is evident from these studies that cellulose microfibrils displayed inherent structural changes in the *cesa1^{aegeus}* and *cesa3^{ixr1-2}* mutants. There seem to be two possible hypotheses to explain how *cesa1^{aegeus}* and *cesa3^{ixr1-2}* mutants create a more amorphous and mobile cellulose-like structure (Fig. 3B). First, the mutated residues may occur in a region of the CESA protein involved in asso-

ciations with other proteins in the CSC (not CESAs), which in turn play a role in microfibril assembly. However, this is only weakly supported by the nature of the *cesa1^{aegeus}* mutation, which is predicted to lie within the fourth transmembrane spanning domain; it would be necessary to invoke a change in conformation state for the interaction with such protein cofactors. Alternatively, the transmembrane region containing mutated residues in *CESA1^{aegeus}* and *CESA3^{ixr1-2}*, while distal to the catalytic site, has been proposed to form a pore in the PM, which facilitates unidirectional glucan passage into the cell wall (36). The mutated residues may be necessary to organize the individual glucan chains into the composite microfibril and thus promote crystallinity (H-bonding) by facilitating association with other glucan chains. This model is consistent with the only reported crystal structure of a CSC, an octameric structure of the periplasmic AxCeSD subunit in the CSC of the bacterium *A. xylinum* in complex with a 5-glucose-cellulose product (37). Here, a dimer interface was necessary to facilitate passage and proper alignment of glucan chains into a crystalline microfibril. If applied to the proposed pore forming transmembrane regions of the plant CESA, this model would suggest that subtle alterations in the transmembrane helix structure via *cesa1^{aegeus}* (A-V) and *cesa3^{ixr1-2}* (T-I) would induce changes in the organization of glucan chains via the inner side of a multimeric subunit association.

Disruption of microfibril assembly induced pharmacologically in bacteria caused an increase in the rate of glucan chain polymerization, illustrating that the two processes are coupled and that crystallization is rate limiting (9, 10). Our results show that *cesa1^{aegeus}* and *cesa3^{ixr1-2}* single mutations displayed higher relative CESA velocity and reduced crystallinity, but were not additive in their effect on velocity in the double mutant. By contrast, more severe defects on cellular expansion were seen in the double mutant. One explanation is that mutated subunits impart influence on the polymerization rates on a single enzyme (CESA) and its catalytic process (β -1,4 glucan synthesis), but that additionally the polymerization rates for individuals do not double in combination (as a CSC) and therefore appear as an intermediate velocity (polymerization) rate. Alternatively, the intermediate CSC velocity in the double mutant could be explained if a direct inhibitory effect of reduced crystallization counteracts some of

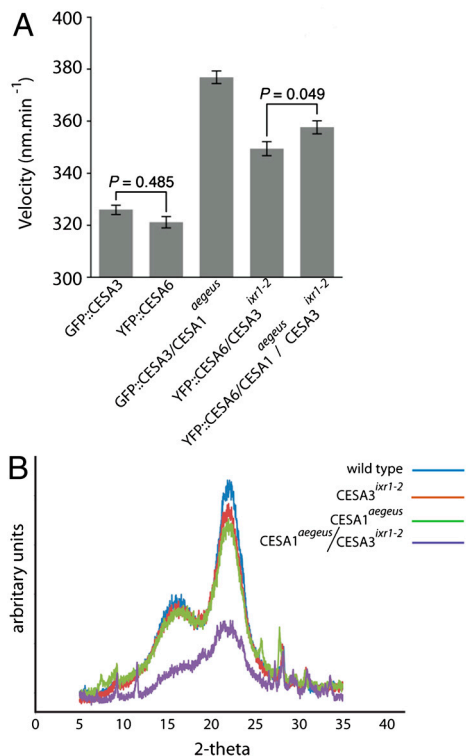


Fig. 4. CESA1^{aegeus} and CESA3^{ixr1-2} mutants display increased CESA particle velocity at the PM focal plane and altered cellulose structure. (A) Epidermal cells of 3-d-old seedling expressing translational fusion reporters were imaged in the upper hypocotyl with spinning disk confocal microscopy (72 frames). CESA complex velocities from the indicated genotypes were compared using ANOVA with Bonferroni tests and significant difference indicated at $P < 0.0001$. Each result represents ≥ 720 CESA complexes from ≥ 10 cells from unique plants. Error bars represent SEM. The mean velocities, from left to right, were 377 ± 2.4 , 349 ± 2.7 , 358 ± 2.5 , 326 ± 1.8 , and 321 ± 2.2 . (B) Analysis of *cesa1^{aegeus}*, *cesa3^{ixr1-2}*, and *cesa1^{aegeus}/cesa3^{ixr1-2}* structural changes in the cellulose fingerprint compared between mutant plants and WT were initially screened by wide-angle XRD using Bragg-Brentano reflective geometries to obtain an RCI: WT = 73.1 ± 1.1 , **cesA3^{ixr1-2}* = 68.7 ± 1.4 , **cesA1^{aegeus}* = 68.4 ± 2.0 , **cesA1^{aegeus}/cesA3^{ixr1-2}* = 65.4 ± 1.8 (* $P < 0.01$ Student's *t* test, $n = 3$).

the indirect (via enhanced rate of polymerization) stimulatory effect of reduced crystallization. Collectively, data from plants appear consistent with bacterial cellulose synthesis (9, 10) and illustrate a biophysical link between crystallinity and polymerization.

The identification of quinoxphen represents a unique cellulose biosynthesis inhibitor (CBI) (Fig. 1 B and C) that induces rapid clearance of YFP::CESA6 from the PM (Fig. 1D), reminiscent of isoxaben (19). While the identification of quinoxphen represents a useful research tool, the resistance loci provide intriguing similarities and differences to isoxaben. Resistance to isoxaben was conferred by mutations in CESA3^{T942I} and CESA6^{R1064W} (26). By contrast, CESA3^{T942I} and CESA6^{R1064W} do not confer quinoxphen resistance, which was mapped to CESA1^{A903V}. Despite subunit specificity, quinoxphen and isoxaben resistance was similarly conferred by mutations in the C-terminal transmembrane spanning region. It is possible that for both CBIs the site of inhibition occurs in this region. The C-terminal transmembrane spanning region has been proposed to mediate subunit association in the CSC (38), and therefore a CBI targeting this region could inhibit CSC formation. Supporting this postulate, live-cell imaging studies revealed clearance of YFP::CESA6 from the PM after quinoxphen treatment, although resistance was conferred by CESA1^{A903V}. Precedence for the observed resistance mechanism whereby drug-binding affinity is

displaced via mutation of residues in a transmembrane spanning region has been observed in the case of hydrophobic sliding for drug resistance in HIV-type 1 protease (39).

In terms of application, if cellulose crystallinity influences the rate of enzymatic hydrolysis (34), cellulose from CESA1^{aegeus} and CESA3^{ixr1-2} (Fig. 3) should be more digestible by a cellulase cocktail. Our results supported this postulate and revealed that mutant cellulose was more readily enzymatically cleaved to individual glucan components. Hence, mutations identified herein could provide insights about how to modify cellulose synthesis *in planta* for improved bioconversion.

Materials and Methods

Chemical libraries used and screening conditions have been described in ref. 20 and supplemental on-line material. Transgenic plants expressing various fluorescent protein tagged genes or gene knockouts were developed by reciprocal crossing and have been described elsewhere (13, 19, 20).

Seedlings expressing GFP::CESA3 or YFP::CESA6 were grown in the dark for 3 d and imaged using spinning disk confocal microscopy, as described previously (26) except a DMI6000 B inverted microscope with Adaptive Focus Control (Leica) was used.

Cell Wall Structural Analysis by XRD. *Arabidopsis* material was prepared and relative crystallinity index (RCI) determined as previously described (35) with a control of synthetic crystalline cellulose (Avicel®, FMC-Biopolymer). Three experimental replicates for mutant and WT biomass samples were performed. Synchrotron X-ray scattering experiments were performed at the macromolecular crystallography beamline F1 of the Cornell High Energy Synchrotron Source. A high-flux wiggler X-ray beam with a photon energy of 13 keV was focused to a spot size of 20 microns using an X-ray focusing capillary with 4 mrad acceptance. Plant samples were mounted in a helium-filled enclosure to reduce air scattering. Due to the high intensity of the microbeam, no further processing was necessary. A Quantum 210 area detector was placed at a distance of 120 mm from the sample, and the full 2D cellulose fiber diffraction image was recorded. Data were integrated using the Fit2D software. Scherrer equation analysis was performed by fitting a Gauss peak to the 200 reflection.

Cell Wall Structural Analysis by ¹³C Magic Angle Spinning SSNMR. For ¹³C solid-state magic angle NMR plants were grown in sterile media supplemented with U-¹³C glucose and ¹⁵N NH₄Cl (100 mM), and cell walls were extracted, desalted, and examined by NMR as previously described (40). ¹³C SSNMR spectra were measured on a Bruker Avance 600 (14.1 T) spectrometer operating at resonance frequencies of 600.13 MHz for ¹H and 150.9 MHz for ¹³C. A double-resonance 4-mm magic-angle-spinning (MAS) probe was used to measure all spectra. Typical radio-frequency field strengths were 62–70 kHz for ¹H decoupling and 50 kHz for ¹³C pulses. The samples were spun under 7- to 12-kHz MAS. ¹³C chemical shifts were referenced to the ¹³CO signal of α -glycine at 176.49 ppm on the TMS scale. For quantitative ¹³C 1D experiments, the ¹³C magnetization was created by direct excitation using a 90° pulse and using a long recycle delay of 20 s. To preferentially detect mobile polysaccharides, a short recycle delay of 2 s was used in the ¹³C direct polarization experiment. ¹³C chemical shifts were assigned by reference with the recently published result (40) and were confirmed by 2D ¹³C-¹³C spin diffusion correlation experiments with a 40-ms mixing time and by 2D J-INADEQUATE experiments (40). The latter correlates ¹³C double-quantum chemical shifts with single-quantum chemical shifts, and gives relatively high spectral resolution.

Additional Details. See *SI Materials and Methods* for additional details.

ACKNOWLEDGMENTS. The authors extend thanks to Herman Hofte, Samantha Vernettes (Institut National de la Recherche Agronomique, France), and Richard Williamson (Australian National University, Canberra, Australia) for supplying genetic material and to Parastoo Azadi (University of Georgia, Athens, GA) and Ulrich English (Macromolecular Diffraction at Cornell High Energy Synchrotron Source, Ithaca, NY) for technical assistance. This work was supported by the National Science Foundation Grants NSF-IOS-0922947 (S.D.), NSF-REU (S.D. and K.C.), PICT2010-0658 (J.M.E.), Department of Energy DOE-FOA 10-0000368 (S.D., D.-M.S., and J.K.C.R.), DE-AC02-07CH11358 (M.H.), and DOE-FG02-03ER20133 (C.R.S.). The Cornell High Energy Synchrotron Source is a national user facility supported by the National Science Foundation and National Institutes of Health/National Institute of General Medical Sciences via National Science Foundation award DMR-0936384.

1. Brown R, Jr, Montezinos D (1976) Cellulose microfibrils: Visualization of biosynthetic and orienting complexes in association with the plasma membrane. *Proc Natl Acad Sci USA* 73:143–147.
2. Tsekos I (1999) The sites of cellulose synthesis in algae: Diversity and evolution of cellulose-synthesizing enzyme complexes. *J Phycol* 35:635–655.
3. Atalla RH, VanderHart DL (1984) Native cellulose: A composite of two distinct crystalline forms. *Science* 223:283–285.
4. Nishiyama Y, Langan P, Chanzy H (2002) Crystal structure and hydrogen-bonding system in cellulose 1b from synchrotron X-ray and neutron fiber diffraction. *J Am Chem Soc* 124:9074–9082.
5. Nishiyama Y, Sugiyama J, Chanzy H, Langan P (2003) Crystal structure and hydrogen bonding system in cellulose 1a from synchrotron X-ray and neutron fibre diffraction. *J Am Chem Soc* 125:14300–14306.
6. Viëtor RJ, Newman RH, Ha M-A, Apperley DC, Jarvis MC (2002) Conformational features of crystal-surface cellulose from higher plants. *Plant J* 30:721–731.
7. Šturcová A, His I, Apperley DC, Sugiyama J, Jarvis MC (2004) Structural details of crystalline cellulose from higher plants. *Biomacromolecules* 5:1333–1339.
8. Jarvis M (2003) Chemistry: Cellulose stacks up. *Nature* 426:611–612.
9. Haigler C, Brown R, Benziman M (1980) Calcofluor white ST Alters the in vivo assembly of cellulose microfibrils. *Science* 210:903–906.
10. Benziman M, Haigler CH, Brown RM, White AR, Cooper KM (1980) Cellulose biogenesis: Polymerization and crystallization are coupled processes in *Acetobacter xylinum*. *Proc Natl Acad Sci USA* 77:6678–6682.
11. Anderson CT, Carroll A, Akhmetova L, Somerville C (2010) Real-time imaging of cellulose reorientation during cell wall expansion in *Arabidopsis* roots. *Plant Physiol* 152:787–796.
12. Richmond T (2000) Higher plant cellulose synthases. *Genome Biol* 1:30011–30016.
13. Desprez T, et al. (2007) Organization of cellulose synthase complexes involved in primary cell wall synthesis in *Arabidopsis thaliana*. *Proc Natl Acad Sci USA* 104:15572–15577.
14. Persson S, et al. (2007) Genetic evidence for three unique components in primary cell-wall cellulose synthase complexes in *Arabidopsis*. *Proc Natl Acad Sci USA* 104:15566–15571.
15. Taylor NG, Howells RM, Huttly AK, Vickers K, Turner SR (2003) Interactions among three distinct CesA proteins essential for cellulose synthesis. *Proc Natl Acad Sci USA* 100:1450–1455.
16. Arioli T, et al. (1998) Molecular analysis of cellulose biosynthesis in *Arabidopsis*. *Science* 279:717–720.
17. Gillmor CS, Poindexter P, Lorieau J, Palcic MM, Somerville C (2002) α -Glucosidase I is required for cellulose biosynthesis and morphogenesis in *Arabidopsis*. *J Cell Biol* 156:1003–1013.
18. Somerville C (2006) Cellulose synthesis in higher plants. *Annu Rev Cell Dev Biol* 22:53–78.
19. Paredez AR, Somerville CR, Ehrhardt DW (2006) Visualization of cellulose synthase demonstrates functional association with microtubules. *Science* 312:1491–1495.
20. DeBolt S, et al. (2007) Morlin, an inhibitor of cortical microtubule dynamics and cellulose synthase movement. *Proc Natl Acad Sci USA* 104:5854–5859.
21. Gu Y, et al. (2010) Identification of a cellulose synthase-associated protein required for cellulose biosynthesis. *Proc Natl Acad Sci USA* 107:12866–12871.
22. Fujita M, et al. (2011) Cortical microtubules optimize cell-wall crystallinity to drive unidirectional growth in *Arabidopsis*. *Plant J* 66:915–928.
23. Bischoff V, et al. (2011) Phytochrome regulation of cellulose synthesis in *Arabidopsis*. *Curr Biol* 21:1822–1827.
24. Chen S, Ehrhardt DW, Somerville C (2010) Mutations of cellulose synthase (CESA1) phosphorylation sites modulate anisotropic cell expansion and bidirectional mobility of cellulose synthase. *Proc Natl Acad Sci USA* 107:17188–17193.
25. Scheible WR, Eshed R, Richmond T, Delmer D, Somerville CR (2001) Modifications of cellulose synthase confer resistance to isoxaben and thiazolidinone herbicides in *Arabidopsis lxr1* mutants. *Proc Natl Acad Sci USA* 98:10079–10084.
26. Desprez T, et al. (2002) Resistance against herbicide isoxaben and cellulose deficiency caused by distinct mutations in same cellulose synthase isoform CESA6. *Plant Physiol* 128:482–490.
27. Gutierrez R, Lindeboom JJ, Paredez AR, Emons AMC, Ehrhardt DW (2009) *Arabidopsis* cortical microtubules position cellulose synthase delivery to the plasma membrane and interact with cellulose synthase trafficking compartments. *Nat Cell Biol* 11:797–806.
28. Segal L, Creely JJ, Martin AE, Conrad CM (1959) An empirical method for estimating the degree of crystallinity of native cellulose using the X-ray diffractometer. *Text Res J* 29:786–794.
29. Andersson S, Serimaa R, Paakkari T, Saranpää P, Pesonen E (2003) Crystallinity of wood and the size of cellulose crystallites in Norway spruce (*Picea abies*). *J Wood Sci* 49:531–537.
30. Thygesen A, Oddershede J, Lilholt H, Thomsen AB, Ståhl K (2005) On the determination of crystallinity and cellulose content in plant fibres. *Cellulose* 12:563–576.
31. Patterson AL (1939) The Scherrer formula for X-ray particle size determination. *Phys Rev* 56:978–982.
32. Fernandes AN, et al. (2011) Nanstructure of cellulose microfibrils in spruce wood. *Proc Natl Acad Sci USA* 108:1195–1203.
33. Newman RH (1999) Estimation of the lateral dimensions of cellulose crystallites using ^{13}C NMR signal strengths. *Solid State Nucl Magn Reson* 15:21–29.
34. Hall M, Bansal P, Lee JH, Reaff MJ, Bommarius AS (2010) Cellulose crystallinity—A key predictor of the enzymatic hydrolysis rate. *FEBS J* 277:1571–1582.
35. Harris D, Stork J, DeBolt S (2009) Genetic modification in cellulose-synthase reduces crystallinity and improves biochemical conversion to fermentable sugar. *Glob Change Biol Bioenergy* 1:51–61.
36. Carpita NC (2011) Update on mechanisms of plant cell wall biosynthesis: How plants make cellulose and other (1 \rightarrow 4)- β -D-glycans. *Plant Physiol* 155:171–184.
37. Hu S-Q, et al. (2010) Structure of bacterial cellulose synthase subunit D octamer with four inner passageways. *Proc Natl Acad Sci USA* 107:17957–17961.
38. Wang J, Howells PA, Cork A, Birch R, Williamson RE (2006) Chimeric proteins suggest that the catalytic and/or C-terminal domains give CesA1 and CesA3 access to their specific sites in the cellulose synthase of primary walls. *Plant Physiol* 142:685–695.
39. Foulkes-Murzycki JE, Scott WRP, Schiffer CA (2007) Hydrophobic sliding: A possible mechanism for drug resistance in human immunodeficiency virus type 1 protease. *Structure* 15:225–233.
40. Dick-Pérez M, et al. (2011) Structure and interactions of plant cell-wall polysaccharides by two- and three-dimensional magic-angle-spinning solid-state NMR. *Biochemistry* 50:989–1000.

Supporting Information

Harris et al. 10.1073/pnas.1200352109

SI Materials and Methods

Plant Material and Growth Conditions. All WT and mutant *Arabidopsis* used were of the Columbia (Col-0) ecotype, and seedlings were germinated and grown as previously described (1). Inhibitors were dissolved in dimethylsulfoxide (DMSO) and added to media so that DMSO never exceeded 0.1% (vol/vol). Isoxaben was purchased from Chem Service Inc. Chemical libraries used and screening conditions have been described in ref. 1 and supplemental on-line material. *ixr1-2* was obtained from the Arabidopsis Biological Resource Center at Ohio State University. Transgenic plants expressing various fluorescent protein tagged genes or gene knockouts were developed by reciprocal crossing and have been described elsewhere (1–3).

Map-Based Cloning of the Quinoxiphen Resistance Locus. Bulk segregant analysis and fine-mapping narrowed the location of the quinoxiphen resistant locus to an 830-kb region between markers UKY3 and NGA1139 that contained the *AtCESA1* gene. Details about the markers are available at The Arabidopsis Information Resource (www.arabidopsis.org). Growth of seed from the F₂ mapping population indicated that heterozygote individuals possessed some degree of resistance to 5.0 μM quinoxiphen as shown by the growth of radially swollen roots suggesting that the *aegeus* mutation confers a semidominant phenotype. To confirm that the mutation found in the *aegeus* mutant was responsible for the quinoxiphen-resistance phenotype, the WT *AtCESA1* gene was transformed into the *aegeus* mutant. T₂ progeny of the *aegeus* mutants transformed with the *AtCESA1* gene segregated for susceptibility on media containing 100 μM quinoxiphen, where only plants homozygous for the *aegeus* mutation can grow.

Cellulose Content Analysis and [¹⁴C]-Glucose Incorporation Assays. Total cellulose content was determined for 7-d-old dark-grown hypocotyls and 8-wk-old stems (5 mg) according to Updegraff (4). For [¹⁴C]-glucose incorporation assays, seeds were germinated and grown in multiwell tissue culture plates at 21 °C in the dark in 2 mL of sterile, liquid MS media containing 0.5% [wt/vol] glucose. After 3 d, the media was replaced with fresh MS media without glucose and containing either 0.05% DMSO or 50 μM quinoxiphen. After 1 h of preincubation with or without inhibitor, 0.5 μCi/mL [¹⁴C]-glucose (American Radiolabeled Chemicals Inc.) was added to each well. The seedlings were incubated for 2 h in the dark at 21 °C and then washed and extracted as described (5).

Microscopy. Seedlings expressing GFP::CESA3 or YFP::CESA6 were grown in the dark for 3 d and imaged using spinning disk confocal microscopy, as described previously (6) except a DMI6000 B inverted microscope with Adaptive Focus Control (Leica) was used. Cells in the upper hypocotyl were imaged at 5-s intervals for 6 min at the plasma membrane. Images were processed to minimize signal from underlying Golgi bodies and to enhance particles at the plasma membrane. A 5-frame running average was applied to the series followed by rolling ball background subtraction (2 pixel radius). Then an FFT bandpass filter was applied to enhance structures of 2–3 pixels (0.32–0.49 μm). Data were analyzed with Imaris software (Bitplane). Cellulose synthase (CESA) particles were detected using the Spots module (estimated diameter = 0.5 μm) and tracked using the Autoregressive Motion algorithm (maximum frame-to-frame distance = 0.067 μm, maximum gap size = 1 frame). CESA velocity was calculated as total displacement divided by duration for tracks with a

duration ≥18 frames (90 s) and straightness ≥0.75. Univariate analysis of variance, with Bonferroni post hoc tests, was performed using SPSS 19 software (IBM) to compare CESA velocities from different genotypes.

Chemical Screening Conditions. Chemical libraries used and screening conditions have been described (1). In brief, approximately 10 sterilized *Arabidopsis* seeds were sown per well, and the plates were incubated in 24-h light (50 μE/m² per s) at 21 °C for 3 d for initial isolation of quinoxiphen. Growth was compared to control wells that contained the same amount of DMSO. Plates were visually scored after 3 d of growth by inspecting each well with a dissecting microscope. Structural analogs were determined using the ChemMine website (<http://bioweb.ucr.edu/ChemMine>) (7) and purchased from ChemBridge. Screening of these compounds for increased potency or any change in phenotype involved germinating seedlings on plates containing half-strength Murashige and Skoog (MS) mineral salts (Sigma-Aldrich), 0.8% agar and after which grown under continuous light (200 μE/m² per s) or in the dark at 21 °C for 7 d.

Analog Analysis for Quinoxiphen, 4-(2-bromo-4,5-dimethoxy-phenyl)-3,4-dihydro-1H-benzo-quinolin-2-one Action Mechanism. To explore the basis for quinoxiphen activity and determine whether a more potent analog could be identified, a structure-based analysis was conducted using tools available through ChemMine (7) and analogs tested for their ability to inhibit root growth (Fig. S1; analogs listed in Table S1). The analog study led to the observation that 5 of the 6 most active compounds contained an arylbromine group associated with a dimethoxy substitution (Fig. S1; compounds 1, 2, 4, 5, 6). The ortho substituted bromine atom is predicted to withdraw charge from the lone aryl group; specifically, the van der Waals interaction of the relatively large bromine atom overlaps with the protons on the CH₂ group adjacent to the carbonyl. To determine whether other electron-withdrawing groups might phenocopy the aryl bromine-containing quinoxiphen, we assayed an additional set of analogs containing bromo, iodo, nitro, and chloro substitutions (Fig. S1). The substitution of bromine with similar electron-spreading atoms resulted in compounds that also caused significantly shorter and more swollen root and hypocotyl cells. The most potent of these compounds were a 2,3-dichloro (compound 3), 2-chloro-6-fluoro (compound 7), 2-fluoro-5-bromo (compound 13), 6-nitro-1,3-benzodioxol (compound 14) or 2-chloro substitution (compound 15) (Fig. S14). Hence, out of 18 compounds that caused reduced root growth, 15 contained a bromo- or related electron-withdrawing substitution. Overall, far greater concentrations of analogs were needed to assay inhibition of radical elongation than was required for quinoxiphen action (25 μM vs. 1–5 μM); hence, quinoxiphen with its specifically positioned aryl bromine was the most effective of the tested compounds for inhibition of radical elongation.

FTIR Analysis. For Fourier transform infrared (FTIR) analysis, dried WT seedlings (3-d old) grown in 5.0 μM quinoxiphen were pooled and homogenized by ball milling. The powder was dried at 30 °C overnight, mixed with KBr, and pressed into 13-mm pellets. Fifteen FTIR spectra for each line were collected on a Thermo Nicolet Nexus 470 spectrometer (ThermoElectric Corporation) over the range 4,000–400 cm⁻¹. For each spectrum, 32 scans were coadded at a resolution of 8 cm⁻¹ for Fourier transform processing and absorbance spectrum calculation by using OMNIC software (Thermo Nicolet). Spectra were corrected for background

by automatic subtraction and saved in JCAMP.DX format for further analysis. Using Win-Das software (Wiley), spectra were baseline-corrected and were normalized and analyzed by using the principal component (PC) analysis covariance matrix method (8). Figures were processed using Sigma Plot (Microsoft).

Callose and Lignin Staining. WT plants were grown for 5 d in the dark on one-half MS agar plates with or without supplementation of 1.0 μM quinoxiphen. Seedlings were directly spread on slides where the staining components were added followed by a coverslip. Callose staining was done with Aniline Blue Fluorochrome (Sigma-Aldrich) at a concentration of 0.1 mg mL^{-1} in 0.07 M sodium phosphate buffer, pH 9. Slides were kept in the dark for 1 h before observation under UV light. Phloroglucinol in a 20% hydrochloric acid solution was used for lignin staining, and slides were observed after 5 min of staining under white light.

Neutral Sugar Analysis of the Quinoxiphen Resistant Mutants. Neutral sugar composition was determined by HPLC from approximately 500 dark-grown hypocotyls from each plant. Cell wall material was prepared from the hypocotyls as described (9) and three replicates of 4 mg of air-dried cell wall material was then prepared for HPLC analysis as described (10).

Glycosyl Linkage Analysis. For glycosyl linkage analysis 1 mg of each sample was prepared in triplicate. The samples were then suspended in 200 μL of dimethyl sulfoxide. The samples were then stirred for 3 d. The samples were permethylated by the treatment with sodium hydroxide and methyl iodide in dry DMSO (11). The samples were subjected to the NaOH base for 15 min, then methyl iodide was added and left for 45 min. The NaOH was then added for 15 min, and finally more methyl iodide was added for 45 min. This addition of more methyl iodide and NaOH base was to insure complete methylation of the polymer. Following sample workup, the permethylated material was hydrolyzed using 2 M trifluoroacetic acid (2 h in sealed tube at 121 $^{\circ}\text{C}$), reduced with NaBD_4 , and acetylated using acetic anhydride/trifluoroacetic acid. The resulting partially methylated alditol acetates (PMAAs) were analyzed on an Agilent 7890 A GC interfaced to a 5975 MSD (mass selective detector, electron impact ionization mode); separation was performed on a 30 m Supelco 2330 bonded phase fused silica capillary column (12).

Enzymatic Digestion and Kinetics of Cellulose Saccharification Efficiency. Identical loadings of semipurified cellulose for wild type, *cesa1^{aegeus}*, and *cesa1^{aegeus}/cesa3^{ivr1-2}*, were analyzed for recalcitrance to saccharification using a commercial cellulase cocktail and compared with the previously measured *cesa3^{ivr1-2}* (13).

The nature of the improved conversion efficiency was quantified by determining pseudoapparent Michaelis–Menten kinetic parameters recognizing that there are inherent ambiguities with an insoluble substrate like cellulose and a multienzyme cellulase cocktail. Nevertheless, using this method we are able to calculate a K_{cat} value, which represents the most effective measure of substrate performance.

Statistical Analyses. Crystalline cellulose content, glycosidic linkage analysis, neutral sugar composition of WT seedlings germinated with quinoxiphen versus mock treatment and WT versus mutant seedlings, root length of WT seedlings germinated with the analogs versus mock treatment, hypocotyl and root length of WT versus mutants and the RCI values and crystallite width determined by XRD of WT and mutant plants were compared by two-tailed Student's *t* tests. The mean velocity of labeled CESA complexes were compared between WT and mutants using a univariate analysis of variance, with Bonferroni post hoc tests.

XRD Analysis. Samples were prepared by oven drying biomass at 60 $^{\circ}\text{C}$ for 36 h. Tissue was then homogenized using an Arthur H. Thomas Company Scientific grinder equipped with a 1-mm sieve. Biomass samples were then contained in a custom built sample holder of pressed boric acid. In brief, plant material was placed into a mold containing a sleeve, and hand pressed with a solid metal plug forming a disk shape. The sleeve and plug were removed, and a boric acid (Fischer) base was then formed by pouring the boric acid over the bottom and sides of the sample and applying 40,000 psi of pressure to the 40 \times 40 mm mold using a Carver Autopellet Press. Samples were pressed to create an even horizontal surface. A Bruker-AXS Discover D8 Diffractometer (Bruker-AXS) was used for wide angle X-ray diffraction with Cu K α radiation generated at 30 mA and 40 kV. The experiments were carried out using Bragg–Brentano geometries (symmetrical reflection). Diffractograms were collected between 2 $^{\circ}$ and 40 $^{\circ}$ with 0.02 $^{\circ}$ resolution and 2-s exposure time interval for each step (run time, 1 h). Sample rotation to redirect the X-ray beam diffraction site was achieved per replicate. *Arabidopsis* material was grown under both greenhouse and growth chamber for analysis. The data analysis was carried out using the calculation for relative crystallinity index (14) of $\text{RCI} = (I_{002} - I_{\text{am}}) / I_{002} \times 100$, where I_{002} is the maximum peak height above baseline at approximately 22.5 $^{\circ}$ and I_{am} is the minimum peak height above the baseline at approximately 18 $^{\circ}$. Diffractograms were collected in Diffract-Plus-XRD Commander software (Bruker-AXS) and minimally processed (baseline identification, noise correction, 3D display, and cropping of RCI signature region) using the EVA and Text-Eval (Bruker-AXS) software.

- DeBolt S, et al. (2007) Morlin, an inhibitor of cortical microtubule dynamics and cellulose synthase movement. *Proc Natl Acad Sci USA* 104:5854–5859.
- Desprez T, et al. (2007) Organization of cellulose synthase complexes involved in primary cell wall synthesis in *Arabidopsis thaliana*. *Proc Natl Acad Sci USA* 104:15572–15577.
- Paredes AR, Somerville CR, Ehrhardt DW (2006) Visualization of cellulose synthase demonstrates functional association with microtubules. *Science* 312:1491–1495.
- Updegraff DM (1969) Semimicro determination of cellulose in biological materials. *Anal. Biochem* 32:420–424.
- Fagard M, et al. (2000) PROCUSTE1 encodes a cellulose synthase required for normal cell elongation specifically in roots and dark-grown hypocotyls of *Arabidopsis*. *Plant Cell* 12:2409–2424.
- Desprez T, et al. (2002) Resistance against herbicide isoxaben and cellulose deficiency caused by distinct mutations in same cellulose synthase isoform CESA6. *Plant Physiol* 128:482–490.
- Girke T, Cheng L-C, Raikhel N (2005) ChemMine. A compound mining database for chemical genomics. *Plant Physiol* 138:573–577.
- Kemsley EK (1998) *Discriminant Analysis of Spectroscopic Data* (John Wiley and Sons, Chichester, UK).
- Dick-Pérez M, et al. (2011) Structure and interactions of plant cell-wall polysaccharides by two- and three-dimensional magic-angle-spinning solid-state NMR. *Biochemistry* 50:989–1000.
- Mendu V, et al. (2011) Subfunctionalization of cellulose synthases in seed coat epidermal cells mediate secondary radial wall synthesis and mucilage attachment. *Plant Physiol* 157:441–453.
- Ciucanu I, Kerek F (1984) A simple and rapid method for the permethylation of carbohydrates. *Carbohydr Res* 131:209–217.
- York WS, Darvill AG, McNeil M, Stevenson TT, Albersheim P (1986) Isolation and characterization of plant cell walls and cell wall components. *Methods in Enzymology*, ed Arthur Weissbach HW (Academic, New York), Vol 118, pp 3–40.
- Harris D, Stork J, DeBolt S (2009) Genetic modification in cellulose-synthase reduces crystallinity and improves biochemical conversion to fermentable sugar. *Glob Change Biol Bioenergy* 1:51–61.
- Segal L, Creely JJ, Martin AE, Conrad CM (1959) An empirical method for estimating the degree of crystallinity of native cellulose using the X-ray diffractometer. *Text Res J* 29:786–794.

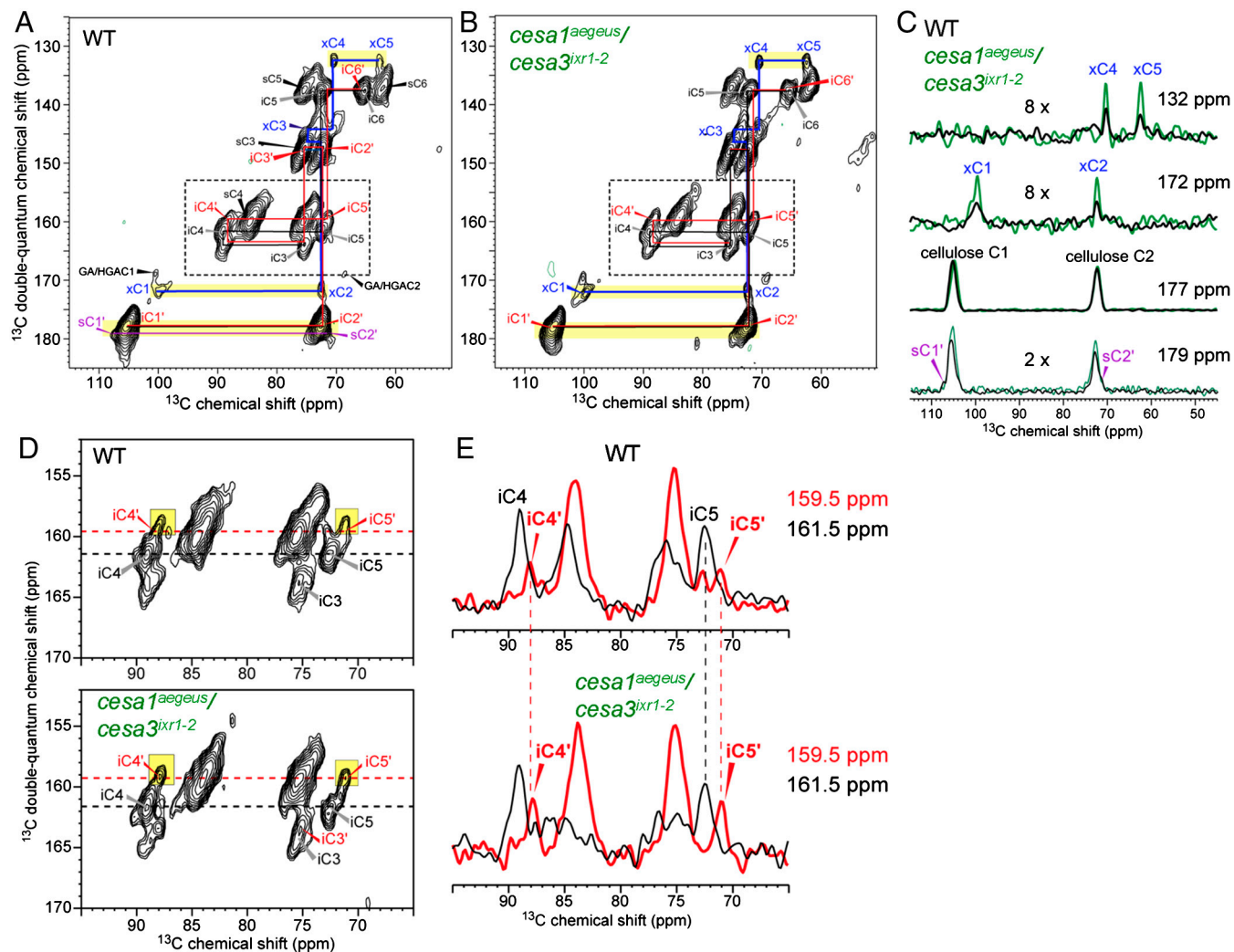


Fig. S6. Two-dimensional ^{13}C double-quantum correlation spectra of WT and *cesa1^{aegeus}/cesa3^{ixr1-2}* cell walls showing changes in the cellulose structure. (A) WT cell wall spectrum. Colored assignments denote polysaccharides whose amounts changed in the double mutant. These include xylose (blue), a modified interior cellulose (red with prime) with different C4 and C5 chemical shifts from those of regular crystalline interior cellulose, and a modified surface cellulose (purple with prime) whose C1 and C2 chemical shifts differ from those of regular surface cellulose. (B) *cesa1^{aegeus}/cesa3^{ixr1-2}* spectrum. The xylose peaks increased in intensity, the modified surface cellulose signals are absent. (C) One-dimensional cross-sections at the specified double-quantum chemical shifts, showing the relative increase of the xylose peak intensities of *cesa1^{aegeus}/cesa3^{ixr1-2}* compared to the WT cell wall and the loss of the modified surface cellulose. (D) Expanded C3-C4 and C4-C5 region of the 2D spectra. The C4' and C5' peaks of the modified interior cellulose are highlighted in yellow. The intensities of this species relative to the regular interior cellulose are higher in the double mutant than in the WT, which is further shown in the (E) 1D cross-sections.

Table S1. Cell wall monosaccharide analysis

| Sugar | Wild type | <i>cesa1^{aegeus}</i> | <i>cesa3^{ixr1-2}</i> | <i>cesa1^{aegeus}/cesa3^{ixr1-2}</i> |
|-----------|--------------|-------------------------------|-------------------------------|--|
| Fucose | 0.57 ± 0.15 | 0.43 ± 0.14 | 0.53 ± 0.06 | 0.68 ± 0.11 |
| Rhamnose | 16.07 ± 0.75 | 14.84 ± 0.37* | 13.70 ± 0.36* | 13.58 ± 0.69* |
| Arabinose | 26.80 ± 0.64 | 21.99 ± 0.91* | 32.46 ± 0.78* | 31.00 ± 3.37* |
| Galactose | 23.69 ± 0.40 | 25.66 ± 0.40* | 25.06 ± 0.83* | 23.41 ± 1.42 |
| Glucose | 2.98 ± 0.24 | 4.35 ± 0.34* | 3.04 ± 0.05 | 3.86 ± 0.05* |
| Mannose | 6.08 ± 0.63 | 6.87 ± 0.75 | 7.28 ± 1.00 | 8.15 ± 1.56 |
| Xylose | 10.43 ± 0.91 | 7.96 ± 0.12* | 8.66 ± 0.51* | 8.59 ± 0.59* |
| GalA | 12.85 ± 0.76 | 9.56 ± 0.39* | 8.91 ± 0.59* | 10.30 ± 0.98* |
| GlucA | 0.53 ± 0.06 | 0.46 ± 0.05 | 0.36 ± 0.06* | 0.42 ± 0.07* |

The results are expressed in mol %. * Indicates changes were significantly different from WT, $P < 0.05$ Student's t test, $n = 3$.

Table S2. Glycosyl linkage analysis

| Linkage | WT | <i>cesa1^{aegeus}/cesa3^{ixr1-2}</i> |
|-------------------------|--------------|--|
| t-Fuc | 0.67 ± 0.06 | 0.60 ± 0.00 |
| t-Rha | 0.70 ± 0.17 | 0.63 ± 0.06 |
| 2-Rha | 1.57 ± 0.15 | 1.23 ± 0.30 |
| 2,4-Rha + 2-Man + 3-Man | 1.63 ± 0.06 | 2.20 ± 0.26* |
| t-Ara | 0.17 ± 0.06 | 0.20 ± 0.00 |
| t-Araf | 2.77 ± 0.85 | 4.07 ± 0.81 |
| 2-Araf | 2.17 ± 0.64 | 1.97 ± 0.15 |
| 3-Araf | 0.83 ± 0.25 | 0.80 ± 0.10 |
| 2,3,4-Ara | 0.30 ± 0.14 | 1.05 ± 1.06 |
| 4-Arap or 5-Araf | 1.87 ± 0.49 | 2.53 ± 0.15* |
| 2,4-Arap or 2,5-Araf | 1.40 ± 0.53 | 1.53 ± 0.15 |
| 3,4-Arap or 3,5-Araf | 0.60 ± 0.20 | 0.97 ± 0.21* |
| t-Xyl | 2.93 ± 0.57 | 2.70 ± 0.35 |
| 4-Xyl | 2.93 ± 0.21 | 2.27 ± 0.28* |
| 2,4-Xyl | 0.83 ± 0.06 | 1.00 ± 0.17 |
| 2,3,4-Xyl | 0.10 ± 0.06 | 0.20 ± 0.14 |
| t-Galf | 0.20 ± 0.10 | 0.30 ± 0.00 |
| t-Gal | 3.33 ± 0.57 | 3.70 ± 0.35 |
| 2-Gal | 1.53 ± 0.15 | 1.40 ± 0.30 |
| 3-Gal | 8.13 ± 1.80 | 11.87 ± 1.46* |
| 4-Gal | 0.83 ± 0.25 | 1.07 ± 0.21 |
| 6-Gal | 0.47 ± 0.06 | 0.63 ± 0.06* |
| 2,3-Gal | 0.23 ± 0.06 | 0.33 ± 0.06 |
| 3,6-Gal | 1.27 ± 0.06 | 2.30 ± 0.20* |
| 4,6-Gal | 0.10 ± 0.00 | 0.17 ± 0.06 |
| 3,4,6-Gal | 0.20 ± 0.10 | 0.27 ± 0.12 |
| t-Glc | 0.53 ± 0.06 | 0.60 ± 0.17 |
| 2-Glc | 0.67 ± 0.35 | 0.77 ± 0.31 |
| 4-Glc | 48.97 ± 4.76 | 41.37 ± 2.17* |
| 2,4-Glc | 0.57 ± 0.21 | 0.43 ± 0.06 |
| 3,4-Glc | 0.47 ± 0.15 | 0.40 ± 0.00 |
| 4,6-Glc | 4.43 ± 0.12 | 3.63 ± 0.50* |
| 3,4,6-Glc | 0.13 ± 0.06 | 0.10 ± 0.00 |
| 2,4,6-Glc | 0.13 ± 0.06 | 0.20 ± 0.17 |
| 2,3,6-Glc | N.D. | 0.10 ± 0.00 |
| t-Man | 1.73 ± 0.38 | 2.40 ± 0.26* |
| 4-Man | 2.73 ± 0.21 | 2.17 ± 0.25* |
| 4,6-Man | 1.63 ± 0.40 | 1.87 ± 0.06 |
| 3,6-Man | 0.37 ± 0.12 | 0.40 ± 0.20 |

The results are expressed in relative %. * Indicates changes were significantly different from WT, $P < 0.05$ Student's t test, $n = 3$.

Table S3. Relative intensities of interior and surface cellulose C4 signals of different cell walls from quantitative ¹³C NMR spectra

| Genotype | I(iC4) 88.5–91.5 ppm | I(sC4) 84–86 ppm | I(iC4)/I(sC4) | Normalized I(iC4)/I(sC4) |
|--|----------------------|------------------|---------------|--------------------------|
| Wild type | 37.7E6 | 58.1E6 | 0.65 | 1.00 |
| <i>cesa1^{aegeus}</i> | 22.4E6 | 32.7E6 | 0.69 | 1.06 |
| <i>cesa3^{ixr1-2}</i> | 25.1E6 | 39.3E6 | 0.64 | 0.98 |
| <i>cesa1^{aegeus}/cesa3^{ixr1-2}</i> | 19.1E6 | 32.0E6 | 0.60 | 0.92 |

cesa1^{aegeus}/cesa3^{ixr1-2} cell wall exhibits a clear reduction in crystallinity.